Honeycomb superperiodic pattern and its fine structure near the armchair edge of graphene observed by low-temperature scanning tunneling microscopy

Ken-ichi Sakai,[1,*] Kazuyuki Takai,[1] Ken-ichi Fukui,[2] Takeshi Nakanishi,[3] and Toshiaki Enoki[1,†]

[1]*Department of Chemistry, Graduate School of Science and Engineering, Tokyo Institute of Technology, 2-12-1 Ookayama, Meguro-ku, Tokyo 152-8551, Japan*

[2]*Department of Materials Engineering Science, Graduate School of Engineering Science, Osaka University, 1-3 Machikaneyama, Toyonaka, Osaka 560-8531, Japan*

[3]*Nanotube Research Center, National Institute of Advanced Industrial Science and Technology, 1-1-1 Higashi, Tsukuba, Ibaraki 305-8565, Japan*

The local electronic structure near a graphene edge was investigated by scanning tunneling microscopy (STM) at low temperature. In addition to the presence of $(\sqrt{3} \times \sqrt{3})R30°$ and honeycomb superperiodic patterns, a fine structure with threefold symmetry was discovered on the individual bright sites in the honeycomb pattern. Electron wave scattering occurring at an armchair edge was confirmed to be responsible for the honeycomb pattern. The fine structure in the honeycomb pattern can be explained by spatial distribution of the local density of states and the following overlap between the atomic orbital of carbon atom and that of STM-tip-end atom, resulting in the threefold-symmetric spatial variation in the tunneling current.

I. INTRODUCTION

Graphene is a one-atom-thick planar sheet of carbon atoms that are densely packed in a honeycomb network. It has an unconventional electronic structure, as is well known from the linear dispersion and massless Dirac Hamiltonian near the Fermi level.[1] Although these features have been known for around 50 years and graphite has been studied intensively both theoretically and experimentally, experimental studies on monolayer graphene have witnessed developments only after the successful micromechanical fabrication of graphene and the discovery of its anomalous quantum Hall effect.[2–4] Nowadays, graphene has attracted considerable attention due to its unconventional electronic properties and as a potential candidate for post-Si electronic devices.

For the development of the nanoscience on graphene, the investigation of nanosized graphene sheet (nanographene) is an important aspect of graphene studies. Such sheet differs from infinite-sized graphene in that they have a graphene edge because their size is sufficiently small to consider the edge contribution. In fact, there are two types of edges; zigzag and armchair edges in finite-sized graphene, and theoretical and experimental studies[5–11] have revealed the existence of a large geometrical effect of the edge shape on the electronic structure of a nanographene sheet. Further, nonbonding π-electron states (edge states) created at zigzag-shaped edges and their localized spins have been found to be responsible for the chemical reactivity and strong magnetic nature of graphene; in contrast, infinite-sized graphene is chemically inert and it exhibits a diamagnetic nature. Interestingly, the structural and chemical modifications of graphene edges allow these features to be modified in various ways.[12–16]

Moreover, the role of the edge as a potential barrier is of particular interest since electron waves are interfered at the edges. In fact, an interference pattern of electron waves appears in scanning tunneling microscopy (STM) images, as observed near the edges on ordinary metal surfaces.[17–19] The interference on graphite has been extensively studied over the last 20 years.[20–24] Nonetheless it remains an important area of investigation. Among others the problem on the relationship between interference patterns and edge structure is the most significant issue, combined with the recent development of the survey of the properties of nanographene. In particular, on the basis of the fact that the detailed edge geometry is suggested to modify the electron-transport behavior due to the various ways of electron scattering dependent of the edge shape in nanographene[25,26] and the interference pattern can be a good fingerprint of the electron scattering, the investigation of the interference is expected to approach the straightforward interpretation of the electron transport as well as the scattering in the vicinity of the graphene edge.

In this work, we report the discovery of threefold-symmetric fine structure appearing on each bright site in a honeycomb superperiodic pattern near the armchair edge of graphene in low-temperature STM (LT-STM) observations, extending our discussion to edge-shape effect of interference pattern. A tight-binding calculation suitably proves the presence of the honeycomb pattern at the armchair edge. The appearance of the fine structure on the honeycomb pattern is demonstrated from the viewpoint of the spatial variation in the tunneling current associated with the spatial distribution of the local density of states (LDOS) and the overlap between the orbitals of carbon atom and STM-tip-end atom.

II. EXPERIMENT

Highly oriented pyrolytic graphite (HOPG) substrates were employed in this study. The experimental targets are step edges on the HOPG surface. As compared to other graphitic materials, HOPG is quite appropriate for this purpose since the richness of its stacking faults gives a graphenelike character to the topmost graphene sheet.[27–29] First, to overcome the difficulty of finding step edges on the cleaved HOPG surface within a narrow scanning area specific to LT-
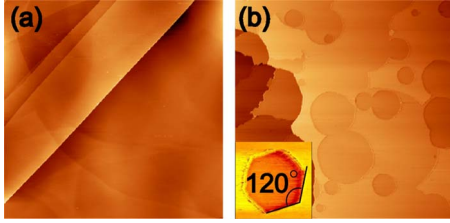
FIG. 1. (Color online) Ambient STM images of (a) cleaved (7×7 μm^2) and (b) heat-treated (900 °C, 2×2 μm^2) HOPG surfaces.

STM, the HOPG substrate was subjected to heat treatment in a furnace in the range of 800–1000 °C for 30 min for the aggressive fabrication of the graphene edge. For this purpose, ion and plasma bombardment or high-temperature heat treatment in air (that is, oxygen-rich condition) has been done in previous reports.[30–32] But we are concerned by their including the possibility of the surface-destructive effect. In this study, to avoid such elements, we took the simple method that highly pure Ar gas (>99.9995%) was fed through the heating system at a flow rate of 1 l/min during this procedure. This allowed us to fabricate edges in a mild condition where the oxygen concentration was well controlled without damaging the sample surface. After heat treatment, the surface structure of the sample was investigated by ambient STM in advance. For LT-STM measurements, the sample was degassed at approximately 200 °C and 10^{-8} Torr for 1 day. STM measurements were performed under UHV condition (at 10^{-11} Torr) at low temperature (9 K) using an LT-STM equipment (UNISOKU, customized) with Pt-Ir tips.

III. RESULTS

Figures 1(a) and 1(b) show ambient STM images of an HOPG surface before and after heat treatment, respectively. A dense packing of step edges is observed on the heat-treated sample surface, whereas the cleaved HOPG surface has only a few step edges. The step edges are created due to the oxidation reaction starting from the chemically active defect sites on the surface during heat treatment. The atomically flat surface, confirmed by the presence of flat zones, always guarantees the observation of atomic-scale images even for the heat-treated sample. This result demonstrates the success of the abovementioned heating procedure, namely, edge fabrication without surface destruction.

Figure 2(a) shows a wide-range LT-STM image observed at 9 K. Heat treatment allowed us to find step edges efficiently. Each step edge was approximately a few graphene layers thick. The atomic-scale image obtained on the terrace near the step edge [indicated by an arrow in Fig. 2(a)] is shown in Fig. 2(b). The step edge lies approximately 1 nm away from the right end of Fig. 2(b). A comparison of the honeycomb network obtained on the terrace with the step direction indicates that the step edge is dominated by an armchair structure [see Figs. 2(a) and 2(b)]. Since this was confirmed frequently on not only the step edges in figures but also the other ones, it can be said that the armchair edge
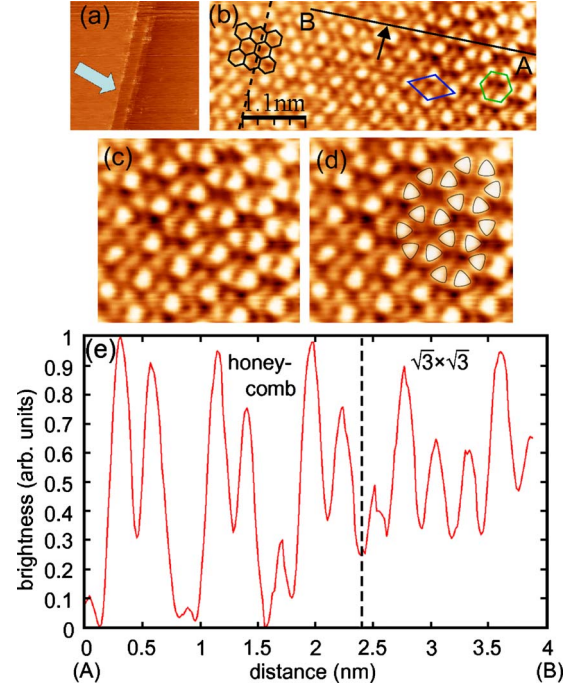

FIG. 2. (Color online) LT-STM images of HOPG surface at 9 K in wide range (a) [78×78 nm^2] and atomic resolution (b) [5.5×1.2 nm^2] taken on the terrace indicated by an arrow in (a). The rhombus, hexagon, and dashed line indicate the unit cells of the $(\sqrt{3} \times \sqrt{3})R30°$ and honeycomb superperiodic patterns and the direction of the step edge observed in (a), respectively. (c) Magnified image of the honeycomb superperiodic pattern (1.4×1.2 nm^2) (d) with an overlaid threefold local symmetry pattern. (e) Cross section taken along the line connecting A and B in (b). The dashed line indicates the boundary between the $(\sqrt{3} \times \sqrt{3})R30°$ and hexagonal patterns pointed by an arrow in (b). The sample bias voltage is 500 mV in (a) and 20 mV in (c)–(e).

is energetically more stable than zigzag one, in agreement with the theoretical prediction.[33] For the features about the atomic image, $(\sqrt{3} \times \sqrt{3})R30°$ and honeycomb superperiodic patterns are observed as shown by unit cells of rhombus and hexagon, respectively. These two structures have already been reported in STM studies of graphite surfaces.[7–10,20–24] However, in this study, a new feature was discovered—a threefold-symmetric local fine structure on individual bright sites in the honeycomb pattern [see Figs. 2(c) and 2(d)]. Since this structure has never been observed in the $(\sqrt{3} \times \sqrt{3})R30°$ pattern or the conventional triangle lattice that can be seen in the interior of the graphite surface, we conclude that fine structure observed is specific to the honeycomb pattern. In addition this phenomenon is completely out of our expectation because π electrons have an isotropic p_z-orbital character along the in-plane direction and are therefore expected to be visualized as the circular structure. For another finding, it should be noted that the amplitude on carbon sites surrounded by bright sites in honeycomb pattern are strongly suppressed while having measurable amplitude in $(\sqrt{3} \times \sqrt{3})R30°$, as evidence by the line profile of Fig. 2(e) taken along the line put on Fig. 2(b). Thereby, from Fig. 2(b), the stronger contrast is confirmed in honeycomb pattern than in $(\sqrt{3} \times \sqrt{3})R30°$.
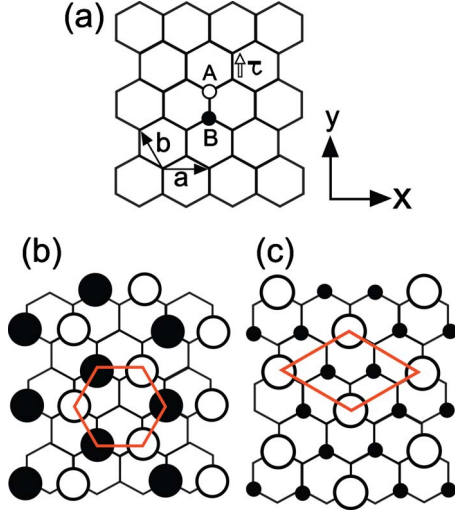
FIG. 3. (Color online) (a) Lattice structure of graphene. y axis is taken parallel to the armchair edge and x axis is perpendicular to it. (b) and (c) shows the 2D squared-amplitude mappings of wave function obtained from Eqs. (6) and (8), respectively. Hexagon and rhombus are the unit cells of honeycomb and $(\sqrt{3} \times \sqrt{3})R30°$ superperiodic patterns. The open and closed circles indicate the difference of the sign of wave function and the size corresponds to the amplitude of the wave function on each site. For the STM measurement, the sites becomes visually enhanced with the increase in the amplitude.

IV. THEORETICAL MODEL AND DISCUSSION

A. Electronic structure of the graphene in the vicinity of the graphene edge

Since STM images mirrors the electronic states of sample surfaces, it is the best way to describe the electronic states of the graphene as a beginning step. Generally the appearance of superperiodic patterns on metal surface can be interpreted on the basis of the interference of plane waves near the Fermi level. Likewise, many studies have already shown that various types of superperiodic patterns observed on graphite surfaces can be well reproduced by the superposition of plane waves corresponding to K and K′ points (corners of the first Brillouin zone)[20–24] and the concept has been valid for a long time. However, it should be recognized that the electronic properties of graphene should be described not by the free-electron model but by the tight-binding model because of the strong p_z-orbital character of the π electron on graphene; wave functions should be expanded by the atomic orbital on each carbon atom as a basis set.

In this section we give the electronic states of the graphene in the vicinity of the Fermi level and the modified ones in the presence of the armchair edge with tight-binding model. Figure 3(a) shows the lattice structure of the graphene, two primitive translation vectors **a** and **b**, and vector τ connecting nearest-neighbor atoms along y direction. In the unit cell there are two carbon atoms, A (open circle) and B (closed circle). The origin of the coordinate is chosen at a B site. Therefore B site is given by $\mathbf{R_B} = n_a \mathbf{a} + n_b \mathbf{b}$ and A site is $\mathbf{R_A} = n_a \mathbf{a} + n_b \mathbf{b} + \tau$ with n_a and n_b being integers and $\tau = (\mathbf{a} + 2\mathbf{b})/3$. In the coordinate system fixed onto the

graphene, we have $\mathbf{a} = a(1,0)$, $\mathbf{b} = a(-1/2, \sqrt{3}/2)$, and $\tau = a(0, 1/\sqrt{3})$ (a is the lattice constant).

The wave function in the vicinity of the Fermi level has only to be taken into account here because of enough low bias voltage (20 mV) applied experimentally. In effective-mass approximation, Schrödinger equation of monolayer graphene in the vicinity of the Fermi level is given as

$$H_0 \mathbf{F}(\mathbf{r}) = \varepsilon \mathbf{F}(\mathbf{r}) \quad (1)$$

with

$$H_0 = \begin{pmatrix} 0 & \gamma(\hat{k}_x - i\hat{k}_y) & 0 & 0 \\ \gamma(\hat{k}_x + i\hat{k}_y) & 0 & 0 & 0 \\ 0 & 0 & 0 & \gamma(\hat{k}_x + i\hat{k}_y) \\ 0 & 0 & \gamma(\hat{k}_x - i\hat{k}_y) & 0 \end{pmatrix},$$

$$(2)$$

where $\mathbf{F}(\mathbf{r})$ is the slowly varying envelope functions on A and B sites at K and K′ points given as

$$\mathbf{F}^K(\mathbf{r}) = \begin{pmatrix} \mathbf{F}_A^K(\mathbf{r}) \\ \mathbf{F}_B^K(\mathbf{r}) \end{pmatrix}, \quad \mathbf{F}^{K'}(\mathbf{r}) = \begin{pmatrix} \mathbf{F}_A^{K'}(\mathbf{r}) \\ \mathbf{F}_B^{K'}(\mathbf{r}) \end{pmatrix} \quad (3)$$

and

$$\mathbf{F}(\mathbf{r}) = \begin{pmatrix} \mathbf{F}^K(\mathbf{r}) \\ \mathbf{F}^{K'}(\mathbf{r}) \end{pmatrix}. \quad (4)$$

$\hat{\mathbf{k}} = (\hat{k}_x, \hat{k}_y) = -i\nabla$ is the wave-number operators and ε is the eigenenergy, given by $\varepsilon = \pm \gamma|\mathbf{k}|$, where $\gamma = \sqrt{3}a\gamma_0/2$ is the band parameter ($-\gamma_0$ is the transfer integral between the nearest-neighbor sites).[34] Using these envelop functions, the wave function in the vicinity of the Fermi level is described as follows:

$$\psi_A(\mathbf{R_A}) = e^{i\mathbf{K} \cdot \mathbf{R_A}} F_A^K(\mathbf{R_A}) + e^{i\mathbf{K'} \mathbf{R_A}} F_A^{K'}(\mathbf{R_A}),$$

$$\psi_B(\mathbf{R_B}) = -\omega e^{i\mathbf{K} \cdot \mathbf{R_B}} F_B^K(\mathbf{R_B}) + e^{i\mathbf{K'} \mathbf{R_B}} F_B^{K'}(\mathbf{R_B}), \quad (5)$$

where ω is the third root ($e^{2\pi i/3}$).

In order to obtain the electronic states of the graphene in the presence of the armchair edge, here let us introduce the contribution of the armchair edge. This can be satisfied by imposing the appropriate initial conditions; as a boundary condition, we assume that the amplitude of the wave function must be zero on the armchair edge. This idea corresponds to the introduction of the infinite potential barrier on armchair edge. Modifying the wave functions under the boundary condition, the wave functions at energy level ε is simply written as

$$\psi_A(\mathbf{R_A}) \approx 0,$$

$$\psi_B(\mathbf{R_B}) \approx C(-e^{i\mathbf{K} \cdot \mathbf{R_B}} + e^{i\mathbf{K'} \cdot \mathbf{R_B}}). \quad (6)$$

where C is the normalization constant. For example, the value of Eq. (6) on typical sites is given by

$$\psi_B(0) \approx 0,$$

$$\psi_B(\mathbf{a}) \approx -\sqrt{3i} \cdot C,$$

$$\psi_B(\mathbf{a} + \mathbf{b}) \approx \sqrt{3i} \cdot C. \qquad (7)$$

The amplitude of the wave function is same and finite value at $\mathbf{a}$, $\mathbf{a}+\mathbf{b}$, and their equivalent sites defined by the basis vectors $\tilde{\mathbf{a}}=-\mathbf{a}-2\mathbf{b}$ and $\tilde{\mathbf{b}}=2\mathbf{a}+\mathbf{b}$. Figure 3(b) shows the two-dimensional (2D) squared-amplitude mapping of wave function obtained from Eq. (6) and is in good agreement with the experimentally observed honeycomb superperiodic pattern (the sites with nonzero amplitude is visible in STM measurement). Here it should be noted that Eq. (6) can be acceptable when the scalar product $\mathbf{k}\cdot\mathbf{r}$ is much smaller than 2π. It means that the superperiodic pattern can be observed only on the terrace near the edge (see Appendix A). As long as this condition is satisfied, the LDOS, which is defined as the summation of the squared amplitude of all wave functions within a certain energy width given by the sample bias and is directly responsible for the STM images, also shows the honeycomb superperiodic pattern like Fig. 3(b) because the electronic states in the vicinity of the Fermi level provided as Eq. (6) is independent of $\mathbf{k}$ and ε. On the other hand, the invisible sites in Fig. 3(b) construct $(\sqrt{3}\times\sqrt{3})R30°$ pattern in Fig. 3(b). Hence it is deduced that $(\sqrt{3}\times\sqrt{3})R30°$ pattern can be duplicated, for example,

$$\psi_B(\mathbf{R}_B) \approx C'(e^{i\mathbf{K}\cdot\mathbf{R}_B} + e^{i\mathbf{K}'\cdot\mathbf{R}_B}). \qquad (8)$$

It is extensively known that the simple combination of K and K′ states causes the $(\sqrt{3}\times\sqrt{3})R30°$ pattern. The values of the wave function on typical sites become

$$\psi_B(0) \approx -2C',$$

$$\psi_B(\mathbf{a}) \approx C',$$

$$\psi_B(\mathbf{a} + \mathbf{b}) \approx C'. \qquad (9)$$

$(\sqrt{3}\times\sqrt{3})R30°$ pattern is confirmed in Fig. 3(c) plotted from Eq. (8). Since the tunneling current is positively correlated with the LDOS at sites, the sites with larger amplitude [open circles in Fig. 3(c)] are visually enhanced.

From Eqs. (6) and (7), only B sites possess the finite value and shows the honeycomb pattern whereas wave function on A sites is almost zero. However, due to the sublattice symmetry of graphene in the presence of the armchair edge, electronic behaviors on A and B sites in real space are symmetric; these patterns should be constructed by not only B sites but also A sites. In calculation, we can derive the wave function having the finite amplitude on A sites and approximately zero on B sites (see Appendix A). Meanwhile, we refer to the distinction about the electronic structure between graphene used in the theoretical part and graphite employed in the experiment. It comes from the interlayer interaction. That is, the sublattice symmetry is broken in AB stacking structure. Consequently one of the sublattices (here they are β sites which are on the center of the hexagonal rings of underneath sheet) is responsible for the electronic states near the Fermi level and the following visualization of STM image. Thus it is reasonable to discuss the experimental result by taking into

account the electronic states on either A or B sites. Here we briefly mention that the interlayer interaction is just attributed to the sublattice selectivity in STM measurement and the electronic states on the visible sites are described on the basis of the graphene regardless of the thickness of substrate (for the details, see Appendix B).

Next, let us extend our discussion to the influence of the edge shape about the superperiodic pattern. The appearance of the superperiodic patterns can be understood qualitatively as follows. The interference pattern is dominated by how electron scatters. As for the graphene, electron scattering at the edge depends on the geometric structure itself, namely, intervalley scattering (K to K′ transition and vice versa) at armchair edge and intravalley scattering (transition around the pristine states) at the zigzag edge. Thus it is expected that the interference pattern appears near the armchair edge because the incident and reflected electron waves are in different states. One can figure out that this can be the reason why the superperiodic patterns are observed near the armchair edge. Indeed, Eqs. (6) and (8) exhibit the linear combination of the electronic states at K and K′ points, indicating the interference of these two different waves as a result of the intervalley scattering. In contrast, intravalley scattering occurring near the zigzag edge causes little change in the electronic states of reflected wave and it is anticipated that no interference pattern can be produced near the zigzag edge, resulting in the conventional triangle lattice. The conclusion is consistent with the LDOS near the zigzag edge characterized by the edge states.[5,6] In this way, we concluded that the superperiodic pattern is decided by the edge structure and thereby the types of the scattering; in the case of the interference observed near the graphene edge, only armchair edge where the intervalley scattering is realized, can be responsible for the superperiodic pattern whereas the zigzag edge causes no interference due to the intravalley scattering.

The distinction of the contrast between two superperiodic patterns seen in Figs. 2(b) and 2(e) can be explained as follows; all of the β-site carbon atoms have a finite amplitude in the $(\sqrt{3}\times\sqrt{3})R30°$ pattern, whereas a subset of the β-carbon atoms have zero in amplitude and the remaining β-carbon atoms have a finite value in the honeycomb pattern. [See Figs. 3(b) and 3(c).] This attributes the large corrugation of the LDOS and it is therefore closely related to the stronger contrast in the honeycomb pattern as observed.

In observation, these superperiodic patterns are observed simultaneously rather than solely like Figs. 3(b) and 3(c). One can notice that we should pay attention the difference between the edge structure used in the model and the experimentally observed. In the model we assume that the uniform armchair edge behaves as the steep potential barrier with infinite energy height. However, in realistic case, carbon atoms at the edge are terminated by various kinds of functional groups (mainly oxygen included) and geometric edge shape consists of the mixture of arbitrary combination between zigzag and armchair ones. Therefore, because the STM observation of such a complicated edge structure unlike an ideal one, it is suggested that the potential barrier is not homogeneous but spatially modulated structure resulting in the interference between K and K′ waves in different manners according to the position-dependent electron scattering.

In Ref. 10, it was demonstrated that the short zigzag (armchair) edge embedded in long armchair (zigzag) edge is important for the coexistence of honeycomb and $(\sqrt{3}\times\sqrt{3})R30°$ patterns (in contrary, coexistence pattern was not predicted at the uniform edge structure). Leastways since both honeycomb and $(\sqrt{3}\times\sqrt{3})R30°$ patterns originate from the interference between K and K′ waves and the superperiodic patterns themselves only depend on how to make the combination of K and K′ waves mathematically, there is the strong possibility of simultaneous appearance of honeycomb and $(\sqrt{3}\times\sqrt{3})R30°$ patterns.

B. STM simulation

Next, we discuss the appearance of the threefold-symmetric fine structure from the viewpoint of the spatial variation in the tunneling current which is monitored in STM measurement. In this study we utilize the calculation method employed in Refs. 35 and 36. Here the tunneling current is defined as the electron hopping between STM-tip-end atom and carbon atom. As a simple model for STM tip, it is assumed that the atom at the end of STM tip has s-orbital behavior. The matrix element t_R in terms of the coupling between the atoms at STM tip end and on surface is given by

$$t_{\mathbf{R}} = t_0 w_{\mathbf{R}} \exp\left(-\frac{d_{\mathbf{R}}}{\lambda}\right)\cos\theta_{\mathbf{R}},$$

$$w_{\mathbf{R}} = \exp(-\alpha^2 d_{\mathbf{R}}^2)\left[\sum_{\mathbf{R}'}\exp(-\alpha^2 d_{\mathbf{R}'}^2)\right]^{-1}, \qquad (10)$$

where t_0 is an unimportant scaling factor, $d_{\mathbf{R}}$ is the distance between the tip and carbon atom, $\theta_{\mathbf{R}}$ is the angle formed by the axis of p_z orbital and the line connecting tip and carbon atom [see Fig. 4(a)], and α is a parameter used for the visual optimization. The hopping integral with parameters λ $=0.085$ nm, $\alpha^{-1}\approx0.13$ nm, and $\Delta=0.5$ nm has been applied in previous works.[35,36] Numerical calculation has been done with these assumptions and the wave functions derived in Sec. IV A.

Figure 4(b) shows the tunneling current mapping for moving the tip position in case that the honeycomb superperiodic pattern can be seen. In this picture every bright sites have the trianglelike threefold-symmetric structure, consequently excellently reproducing the structure observed. The result is attributed to two factors. One is the threefold-symmetric LDOS distribution. This leads to the same situation about the overlap between STM-tip-end and carbon atoms by 120° rotation of STM-tip centered with a bright site. Another is the antibonding coupling between nearest-neighbor bright sites mediated by STM tip due to the opposite phase on these sites [see Fig. 3(b)], that is, the destructive interference and following generation of the nodes on the middle of the bright sites. Meanwhile, in the same manner, it is also expected that the sixfold (threefold) symmetric structure appears on visible larger (smaller) amplitude bright sites in $(\sqrt{3}\times\sqrt{3})R30°$ pattern. The simulation result gives that, as expected, slightly hexagonlike and well-defined trianglelike structures can be verified from the current mapping drawn on Fig. 4(c).
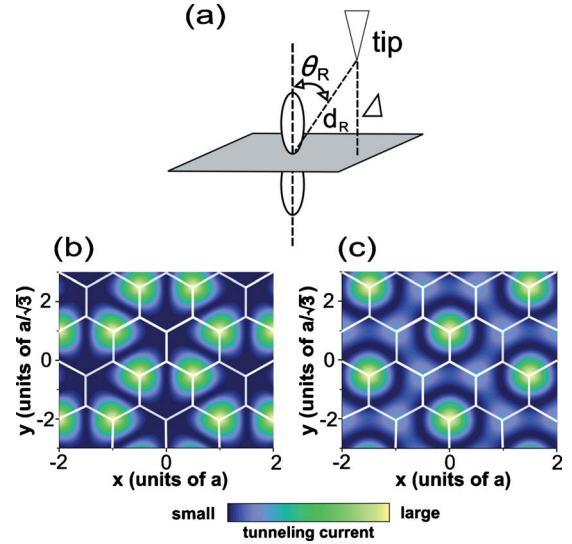

FIG. 4. (Color online) (a) Geometric arrangement of STM tip and sample surface for the STM simulation. Elliptic pictures idicate lobe of p_z orbital on carbon site. Δ is the perpendicular distance between STM tip and graphene sheet (this parameter has constant value, hence the height of the STM tip is assumed to be fixed). (b) and (c) 2D current mappings of honeycomb and $(\sqrt{3}\times\sqrt{3})R30°$ superperiodic patterns. The tunneling current increases with the color variation along with idigo blue (black), green (gray), and pale yellow (white) (in arbitrary unit).

It is widely accepted that the structure observed in STM measurement gives us the information about the spatial behavior of the surface electronic states in real space. Therefore it is also reasonable to take the fine structure as the local symmetry of the wave function on sites. In the honeycomb pattern, when we focus on a particular bright site, this site is subjected to repulsive force from three nearest-neighbor bright sites which have high electron density (the amplitude of the wave function on each site can be the measure of the electron density at their sites). Hence, it is assumed that the shape of the wave functions on the bright sites is transformed from circular specific to p_z orbital to threefold-symmetric structure because of compression by Coulomb repulsion from their three nearest-neighbor bright sites. This idea provides the same conclusion as that obtained from the viewpoint of the spatial variation in the tunneling current mentioned before. It is, however, known that the Coulomb repulsion on a graphene sheet is not sufficiently strong to affect the change in the symmetry of the wave function. Therefore, this is not the case in graphene.

Finally, the STM images are also affected by the tip's shape. For this study the fine structure can be observed even when the tip and sample were changed. We concluded that a tip-shape effect is not expected.

The discussion given reminds us that the truly drawn picture in STM image is the mapping of the tunneling current, not direct translation of the corrugation of LDOS. The local fine structure observed in our research is also just appearance according to the spatial variation in the tunneling current. In addition this can be realized by the contribution of the STM tip because the distance between nearest-neighbor bright site are too far for the orbital coupling.

V. SUMMARY

In summary, a honeycomb superperiodic pattern is observed in LT-STM measurements in the vicinity of an armchair edge on a heat-treated HOPG surface. We reveal that the appearance of the superperiodic patterns is specific to the electronic state in the vicinity of the armchair edge where the incident and reflected waves have chance to interfere each other due to the intervalley scattering, despite the absence near the zigzag case due to the intravalley scattering. Furthermore, the distinct appearance of a threefold-symmetric local fine structure is discovered on the individual bright sites in the honeycomb pattern. We made clear that the fine structure is theoretically reproduced well by mapping the tunneling current. This is ascribed to the threefold-symmetric spatial LDOS distribution and the following destructive interference between nearest-neighbor bright sites mediated by the atomic orbital of STM-tip-end atom. We would like to emphasize that we have undoubtedly succeeded in the visualization of the electronic properties related to the armchair graphene edge.

ACKNOWLEDGMENTS

APPENDIX A: DETAILS OF THE ELECTRONIC STATES OF THE GRAPHENE IN THE VICINITY OF THE ARMCHAIR EDGE

Solving the Schrödinger equation of single-layer graphene [Eqs. (1)–(4)], we have

$$\begin{pmatrix} F_A^K(\mathbf{r}) \\ F_B^K(\mathbf{r}) \end{pmatrix} = N_K \begin{pmatrix} \pm k_-^K/|\mathbf{k}| \\ 1 \end{pmatrix} e^{i(k_x^K x + k_y^K y)} \tag{A1}$$

for K point and

$$\begin{pmatrix} F_A^{K'}(\mathbf{r}) \\ F_B^{K'}(\mathbf{r}) \end{pmatrix} = N_{K'} \begin{pmatrix} \pm k_+^{K'}/|\mathbf{k}| \\ 1 \end{pmatrix} e^{i(k_x^{K'} x + k_y^{K'} y)} \tag{A2}$$

for K′ point, where N_j is normalization constants, and $k_\pm^j = k_x^j \pm i k_y^j$ ($j = $ K and K′), respectively.

Here let us impose the boundary condition already referred. For the general expression of the armchair edge, we write this as $\psi_A[\boldsymbol{\tau} + n(\mathbf{a}+2\mathbf{b})] = \psi_B[n(\mathbf{a}+2\mathbf{b})] = 0$ with integer n. Substituting Eqs. (A1) and (A2) into this condition, we obtain $N_{K'} = \omega N_K$, $k_x^K = -k_x^{K'}$, and $k_y^K = k_y^{K'}$. The electronic states at energy ε are obtained from the summation of wave functions in terms of all wave vectors $\mathbf{k}$. Here let us take the additional linear combination of the states corresponding to $\mathbf{k}$ and $-\mathbf{k}$ and then integrate this paired function all over the considerable $\mathbf{k}$ at ε. When $|\mathbf{k}|$ is sufficiently small against that of K and K′, Eq. (6) is precisely correct on the origina

l point. For the approximate validity, the condition $\mathbf{k} \cdot \mathbf{r} \ll 2\pi$ is needed to be satisfied. Naturally there is arbitrary property for putting the original point. From the experimental result that the superperiodic pattern is observed in the vicinity of the edge, it is appropriate to put the original point on the carbon sites near the edge. If the Fermi level before the application of bias voltage (20 mV) is on the Dirac point, the approximate expression of Eq. (6) is valid in the range of 3 nm around the original point. Hence the superperiodic pattern is expected to be confirmed only on the terrace in the vicinity of the graphene edge.

In contrast, in case of the negative combination Eq. (6) is modified as follows:

$$\psi_A(\mathbf{R_A}) \approx C''(e^{i\mathbf{K} \cdot \mathbf{R_A}} - \omega e^{i\mathbf{K}' \cdot \mathbf{R_A}}),$$

$$\psi_B(\mathbf{R}_B) \approx 0. \tag{A3}$$

And the values on typical sites are

$$\psi_A(\boldsymbol{\tau}) \approx 0,$$

$$\psi_A(\boldsymbol{\tau} + \mathbf{a}) \approx \sqrt{3} i\omega \cdot C'',$$

$$\psi_A(\boldsymbol{\tau} + \mathbf{a} + \mathbf{b}) \approx -\sqrt{3} i\omega \cdot C''. \tag{A4}$$

Since Eqs. (6) and (A3) are degenerated at energy ε, it is demonstrated that the sublattice symmetry is restored.

APPENDIX B: COMPARISON OF THE ELECTRONIC STRUCTURE BETWEEN GRAPHENE AND GRAPHITE

One can raise the issue of graphite vs graphene since the graphene is used as the model for our theoretical analysis although the experimentally employed sample was graphite. Here we demonstrate that the electronic structure of the graphite surface near the Fermi level can be described in the same manner as that of the graphene on either A or B sites. For the clear understanding and the introduction of the effect of interlayer hopping, we adopt the bilayer graphene as the model. From the basic tight-binding model, the Schrödinger equation of bilayer graphene is given by

$$-\gamma_0 \sum \psi_{A1}(\mathbf{R}_{A1}) - \gamma_1 \psi_{B1}(\mathbf{R}_{B1}) = \varepsilon \psi_{A2}(\mathbf{R}_{A2}) \approx 0, \tag{B1}$$

where A1 and B1 (A2 and B2) indicates the A and B sites on upper (lower) graphene sheet, B1 and A2 corresponds to α sites, $\mathbf{R}_{A1}$ is the position vector of three nearest-neighbor A1 sites of a certain B1 site, and $-\gamma_1$ is a interlayer transfer integral between B1 and A2 sites. In the vicinity of the Fermi level sufficiently below $-\gamma_1$(0.35 eV), the electronic states are occupied by π electrons on A1 and B2 sites (as we mentioned, graphite is also the same case). It means that the amplitude on B1 and A2 sites are negligible. Then the term of $-\gamma_1$ can be removed from Eq. (B1) and we obtain the same equation as monolayer's case. Furthermore, the term of $-\gamma_0$ is common regardless of the thickness of graphene. We

point out that the electronic states on graphite substrate can be explained on the basis of that of the graphene and the role of interlayer interaction is only for selecting the visible sites. In other words, even if the graphite was employed in the experiment, we can discuss the electronic states on the graphite surface with the basis of graphene without losing any essences. The topmost graphene sheet can be identified as the sheet interacting with the graphite substrate.

*sakai.k.ab@m.titech.ac.jp

†enoki.t.aa@m.titech.ac.jp

[1] J. C. Slonczewski and P. R. Weiss, Phys. Rev. **109**, 272 (1958).

[2] K. S. Novoselov, A. K. Geim, S. V. Morozov, D. Jiang, Y. Zhang, S. V. Dubonos, I. V. Grigorieva, and A. A. Firsov, Science **306**, 666 (2004).

[3] K. S. Novoselov, A. K. Geim, S. V. Morozov, D. Jiang, Y. Zhang, S. V. Dubonos, I. V. Grigorieva, and A. A. Firsov, Nature (London) **438**, 197 (2005).

[4] Y. Zhang, Y. Tan, Ht. L. Stormer, and P. Kim, Nature (London) **438**, 201 (2005).

[5] M. Fujita, K. Wakabayashi, K. Nakada, and K. Kusakabe, J. Phys. Soc. Jpn. **65**, 1920 (1996).

[6] K. Wakabayashi, M. Fujita, H. Ajiki, and M. Sigrist, Phys. Rev. B **59**, 8271 (1999).

[7] Y. Kobayashi, K. Fukui, T. Enoki, K. Kusakabe, and Y. Kaburagi, Phys. Rev. B **71**, 193406 (2005).

[8] Y. Kobayashi, K. Fukui, T. Enoki, and K. Kusakabe, Phys. Rev. B **73**, 125415 (2006).

[9] T. Enoki, Y. Kobayashi, and K. Fukui, Int. Rev. Phys. Chem. **26**, 609 (2007).

[10] Y. Niimi, T. Matsui, H. Kambara, K. Tagami, M. Tsukada, and H. Fukuyama, Phys. Rev. B **73**, 085421 (2006).

[11] Z. Kluzek, Z. Wapar, E. A. Denisov, T. N. Kompaniets, I. V. Makarenko, A. N. Titkov, and A. S. Bhatti, Appl. Surf. Sci. **161**, 508 (2000).

[12] K. Nakada, M. Fujita, G. Dresselhaus, and M. Dresselhaus, Phys. Rev. B **54**, 17954 (1996).

[13] M. Maruyama and K. Kusakabe, J. Phys. Soc. Jpn. **73**, 656 (2004).

[14] F. Cervantes-Sodi, G. Csányi, S. Piscanec, and A. C. Ferrari, Phys. Rev. B **77**, 165427 (2008).

[15] K. Takai, H. Sato, T. Enoki, N. Yoshida, F. Okino, H. Touhara, and M. Endo, J. Phys. Soc. Jpn. **70**, 175 (2001).

[16] K. Takai, H. Kumagai, H. Sato, and T. Enoki, Phys. Rev. B **73**, 035435 (2006).

[17] M. F. Crommie, C. P. Lutz, and D. M. Eigler, Nature (London) **363**, 524 (1993).

[18] L. Petersen, P. Laitenberger, E. Lægsgaard, and F. Besenbacher, Phys. Rev. B **58**, 7361 (1998).

[19] Y. Hasegawa and Ph. Avouris, Phys. Rev. Lett. **71**, 1071 (1993).

[20] P. L. Giunta and S. P. Kelty, J. Chem. Phys. **114**, 1807 (2001).

[21] T. Tapasztó, P. Nemes-Incae, Z. Osváth, M. C. Bein, Al. Darabont, and L. P. Biró, Physica E **40**, 2263 (2008).

[22] P. Ruffieux, M. Mello-Franco, O. Gröning, M. Bielmann, F. Zerbetto, and P. Gröning, Phys. Rev. B **71**, 153403 (2005).

[23] J. Valenzuela-Benavides and L. Morales de la Garza, Surf. Sci. **330**, 227 (1995).

[24] G. M. Shedd and P. E. Russell, Surf. Sci. **266**, 259 (1992).

[25] K. Wakabayashi, Phys. Rev. B **64**, 125428 (2001).

[26] X. Jia, M. Hofmann, V. Meunier, B. G. Sumpter, J. Campos-Delgado, J. M. Romo-Herrera, H. Son, Y.-P. Hsieh, A. Reina, J. Kong, M. Terrones, and M. S. Dresselhaus, Science **323**, 1701 (2009).

[27] T. Matsui, H. Kambara, Y. Niimi, K. Tagami, M. Tsukada, and H. Fukuyama, Phys. Rev. Lett. **94**, 226403 (2005).

[28] G. Li, A. Luican, and E. Andrei, Phys. Rev. Lett. **102**, 176804 (2009).

[29] G. Li and E. Andrei, Nat. Phys. **3**, 623 (2007).

[30] A. Tracz, A. A. Kalachev, G. Wegner, and J. P. Rabe, Langmuir **11**, 2840 (1995).

[31] V. J. Cee, D. L. Patrick, and T. P. Beebe, Jr., Surf. Sci. **329**, 141 (1995).

[32] Y. Zhu, J. D. Mcbride, T. A. Hansen, and T. P. Beebe, Jr., J. Phys. Chem. B **105**, 2010 (2001).

[33] S. Okada, Phys. Rev. B **77**, 041408(R) (2008).

[34] T. Ando, J. Phys. Soc. Jpn. **74**, 777 (2005).

[35] T. Nakanishi and T. Ando, J. Phys. Soc. Jpn. **77**, 024703 (2008).

[36] V. Meunier and Ph. Rambin, Phys. Rev. Lett. **81**, 5588 (1998).